JBC RESEARCH ARTICLE

Mechanism of chorismate dehydratase MqnA, the first enzyme of the futalosine pathway, proceeds *via* substrate-assisted catalysis

Received for publication, May 5, 2022, and in revised form, October 10, 2022 Published, Papers in Press, October 18, 2022,
https://doi.org/10.1016/j.jbc.2022.102601

Archna Prasad[1], **Constanze Breithaupt**[1], **Duc-Anh Nguyen**[1], **Hauke Lilie**[1], **Jörg Ziegler**[2], **and Milton T. Stubbs**[1,*]

From the [1]*Institut für Biochemie und Biotechnologie, Charles-Tanford-Proteinzentrum, Martin-Luther-Universität – Halle-Wittenberg, Halle/Saale, Germany;* [2]*Abteilung Molekulare Signalverarbeitung, Leibniz-Institut für Pflanzenbiochemie, Halle/Saale, Germany*

Edited by Joseph Jez

MqnA, the only chorismate dehydratase known so far, catalyzes the initial step in the biosynthesis of menaquinone *via* the futalosine pathway. Details of the MqnA reaction mechanism remain unclear. Here, we present crystal structures of *Streptomyces coelicolor* MqnA and its active site mutants in complex with chorismate and the product 3-enolpyruvyl-benzoate, produced during heterologous expression in *Escherichia coli*. Together with activity studies, our data are in line with dehydration proceeding *via* substrate assisted catalysis, with the enol pyruvyl group of chorismate acting as catalytic base. Surprisingly, structures of the mutant Asn17Asp with co-purified ligand suggest that the enzyme converts to a hydrolase by serendipitous positioning of the carboxyl group. All complex structures presented here exhibit a closed Venus flytrap fold, with the enzyme exploiting the characteristic ligand binding properties of the fold for specific substrate binding and catalysis. The conformational rearrangements that facilitate complete burial of substrate/product, with accompanying topological changes to the enzyme surface, could foster substrate channeling within the biosynthetic pathway.

In prokaryotes, ubiquinone and menaquinone serve as electron carriers in the electron transport chain (1). Although some prokaryotes utilize ubiquinone solely, mycobacteria and most gram-positive bacteria produce menaquinone exclusively, and many gram-negative bacteria such as *Escherichia coli* switch from ubiquinone to menaquinone when grown under anaerobic conditions (2). In humans, menaquinone (vitamin K_2) acts as a cosubstrate in the carboxylation of glutamic acids that leads to the activation of proteins essential for blood coagulation, control of cell growth, apoptosis, signal transduction, and calcium metabolism (3). As *de novo* biosynthesis of menaquinone is performed only by prokaryotes, humans must acquire menaquinone through diet, intestinal bacterial synthesis, or conversion of plant-derived phylloquinone (vitamin K_1).

Two distinct pathways of menaquinone biosynthesis have been described in bacteria (Fig. 1): the classical *o*-succinylbenzoate pathway that has been studied extensively in *E. coli* (4, 5) and the more recently discovered futalosine pathway (6). Phylogenetic analyses suggest that the futalosine pathway evolved earlier than the *o*-succinylbenzoate pathway (7). The former was found in nearly one third of all menaquinone producing prokaryotes analyzed, including pathogenic bacteria like *Helicobacter pylori, Campylobacter jejuni*, *Chlamydiae*, and spirochetes, but not in important commensal bacteria including lactobacilli. Enzymes involved in this pathway are therefore potential targets for the development of new antibiotics (8).

MqnA is the first enzyme of the futalosine pathway (6, 9–12), catalyzing the dehydration of chorismate to yield 3-enolpyruvyl-benzoate (3-EPB), a reaction not observed for any other enzyme so far (Fig. 1). Chorismate is the product of the shikimate pathway and the precursor of many aromatic compounds including the amino acids phenylalanine, tyrosine, and tryptophan, the folate coenzymes, the iron chelating siderophores in addition to the electron carriers ubiquinone and menaquinone (Fig. S1). As enzymes of the shikimate pathway—as well as enzymes that convert chorismate—are present only in bacteria, fungi, and plants, they are likewise promising targets for potential antimicrobials and herbicides.

Crystal structures of MqnA from *Streptomyces coelicolor* (*Sc*MqnA) and *Deinococcus radiodurans* (*Dr*MqnA) solved initially as "proteins of unknown function" as part of the Structural Genomics Initiative (12), revealed an overall fold reminiscent of periplasmic binding proteins. Sequence conservation in these structures, as well as recent analyses of *Dr*MqnA from *D. radiodurans* in complex with a putative substrate analog 3-hydroxy-benzoate (3-HBA) suggest that the active site of MqnA is located in a deep cleft in the center of the enzyme (13).

Here we present high-resolution crystal structures of *Sc*MqnA in complex with the product 3-EPB, as well as mutants in complex with the chorismate substrate and the presumed hydrolysis product 3,4-dihydroxycyclohexa-1,5-dienoate (3,4-CHD), and show that substrate and products bind in a manner completely different to the ligand 3-HBA. Our structural data, combined with enzyme activity studies of MqnA and its mutants, allow elucidation of the unusual

* For correspondence: Milton T. Stubbs, stubbs@biochemtech.uni-halle.de.
Present address for Archna Prasad: Proteros biostructures GmbH, Bunsenstr. 7a, D - 82,152 Martinsried, Germany.

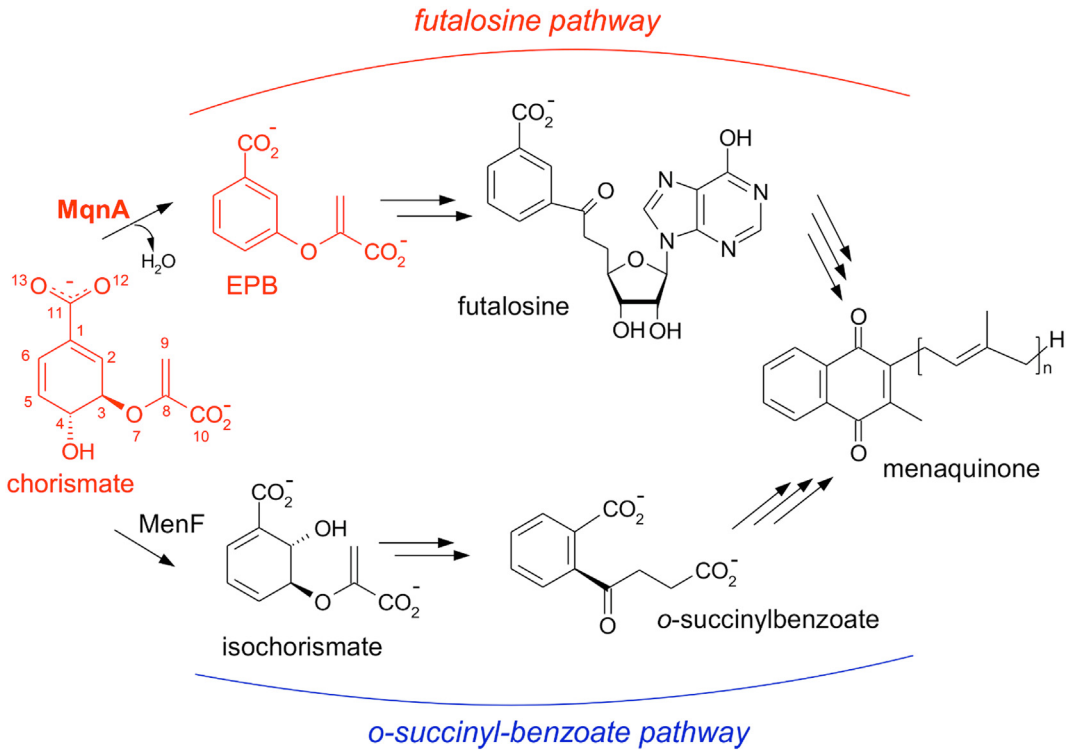

Figure 1. MqnA (chorismate dehydratase) catalyzes the first step in the biosynthesis of menaquinone *via* the futalosine pathway. The corresponding step in the "classical" *o*-succinylbenzoate pathway is catalyzed by the isochorismate synthase MenF.

reaction mechanism of MqnA. In all structures presented here, the bound substrates and products are shielded completely from bulk solvent, indicating that substrate access and product release require "opening" of the active site cleft. Although MqnA adopts a Venus flytrap (VFT) fold found typically in ligand binding proteins, the degree of opening/closing in MqnA (and probably other enzymes) appears to be different to those of their nonenzymatic structural neighbors.

Results and discussion

ScMqnA is a homodimer

Recombinant *Sc*MqnA purified from *E. coli* crystallized in two crystal forms (monoclinic with space group $P2_1$ and orthorhombic with space group $P2_12_12_1$) that diffracted to resolutions of 1.9 Å and 2.2 Å, respectively (see Table S1 for data collection and refinement statistics), with both forms containing two molecules in the asymmetric unit. In each case, the two molecules of *Sc*MqnA are related by an 180.3° rotation (Fig. S2*A*), with a buried surface area of 2150 $Å^2$ (a size that is typical for protein–protein complexes and well above values observed for crystal contacts of monomeric proteins (14)), involving 63 amino acids in the interface. The same interaction is observed between chain A/D and B/C of the four molecules in the asymmetric unit of the earlier structure of *Sc*MqnA (2nxo, (12)). Sedimentation equilibrium ultracentrifugation (Fig. S2*B*) confirmed the presence of an *Sc*MqnA dimer in solution, with a molecular weight of 62 kDa (theoretical monomer mass 31.4 kDa). Chains A and B of the monoclinic form as well as chain B of the orthorhombic form are well defined in their entirety and superimpose well upon one another, whereas electron density for residues 107 to 112 is less well defined in orthorhombic chain A, indicating the presence of more than one conformation (Fig. S3). This is accompanied by a significant upward shift of 1.3 Å in strand β7, helix α5, and the connecting loop (encompassing residues 129–143) compared to all three other chains. Data and figures in the text are based on the monoclinic structure unless otherwise stated.

Overall structure of ScMqnA

*Sc*MqnA adopts a VFT fold consisting of two similar lobes interconnected by two linkers (Fig. 2*A*) (15, 16). The two lobes are each composed of a mixed β-sheet flanked on both sides by α-helices, with a topology $2_\uparrow1_\uparrow3_\uparrow5_\downarrow4_\uparrow$ typical of the SCOP superfamily of periplasmic binding protein-like structures type II. As in other VFT proteins, the C-terminal lobe (lobe 2) is inserted after the fourth β-strand of the N-terminal lobe (lobe 1). The two lobes of MqnA are followed by an uncommon 90 amino acid long α-helical region (α-clamp) that wraps around the back of lobe 1. *Sc*MqnA strand β4 is interrupted by a four amino acid loop (Phe73-Ala77) that protrudes from lobe one into the α-clamp, where it makes numerous hydrophobic contacts to amino acids of helix α9, the C terminus, and the loop connecting α11 and α12. Also unusual is a π-bulge in the middle of helix α6 (at Ile160) of lobe two that allows additional hydrophobic interactions between α6 and the α-clamp. The dimer is formed largely by interactions of the N-terminal

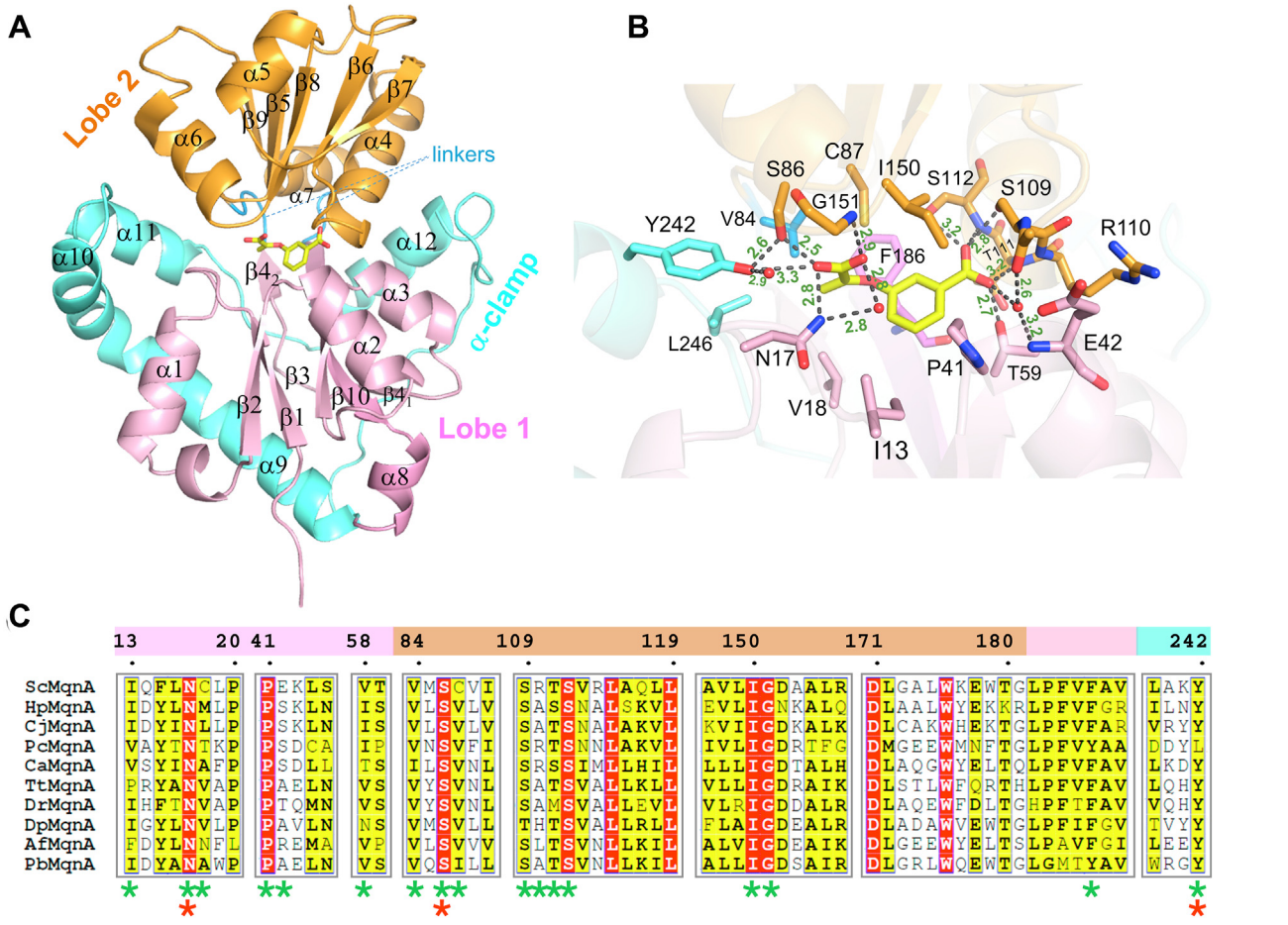

Figure 2. Overall structure of *Sc*MqnA and its active site. *A*, cartoon representation of the overall structure of *Sc*MqnA. The N-terminal lobe one is colored *light pink*, the second lobe is colored *orange*, and the C-terminal α-clamp *cyan*. The two linker regions connecting the two lobes are shown in blue. The MqnA product 3-enolpyruvyl-benzoate (3-EPB) binds to the active site that is buried between the two lobes. *B*, close-up view of the *Sc*MqnA active site. Amino acids that form the binding pocket are shown as *sticks*, coloring corresponds to panel A. 3-EPB is shown as *yellow stick model*, and water molecules are *red spheres*. Hydrogen bonds are represented as *black dashed lines* with distances (Å) indicated. Amino acids of the pocket that do not form hydrogen bonds are mainly involved in hydrophobic interactions. *C*, selected regions of MqnA sequence conservation from various organisms (Sc: *Streptomyces coelicolor*; Hp: *Helicobacter pylori*; Cj: *Campylobacter jejuni*; Pc: *Pedobacter cryoconitis*; Ca: *Chlamydia abortus*; Tt: *Thermus thermophilus*; Dr: *Deinococcus radiodurans*; Dp: *Desulfovibrio piger*; Af: *Archaeoglobus fulgidus*; Pb: *Paenibacillus beijingensis*). Color bars above the alignment correspond to structure elements as in (A). Completely conserved and partially conserved amino acids are shaded in *red* and *yellow*, respectively. Active site amino acids that are involved in the interaction with 3-EPB (including hydrophobic interactions) are indicated with a *green star*. *Red stars* indicate catalytically important amino acids. See Fig. S6 for complete sequences. *Sc*MqnA, MqnA from *Streptomyces coelicolor*.

amino acids with helix α11 and the succeeding loop of the second molecule, as well as of amino acids 19 to 38 (containing β2 and α1) with the equivalent region of the second molecule. As the dimer interface is distant from the active site and from the moving regions in VFT proteins, it is not expected to influence catalysis.

Electron density of copurified ligand reveals product complex

During model building, additional electron density observed in both crystal forms could be assigned to the product of chorismate dehydration, 3-EPB (Figs. 2*B* and 3*A*) in a cavity at the interface between the two lobes corresponding to the ligand binding site in periplasmic binding proteins. As neither chorismate nor 3-EPB were added to MqnA before or during crystallization (and 3-EPB has not been reported as a metabolite in *E. coli* (17)), we conclude that the recombinant MqnA must have converted chorismate, abundant in *E. coli* cells, into 3-EPB that then remained bound in the active site. The presence of 3-EPB in purified MqnA was additionally confirmed by liquid chromatography/mass spectrometry (LC-MS/MS) analysis (Fig. S4 and Table S2), where mass spectra and retention times were indistinguishable from the compound generated by incubation of *Sc*MqnA with chorismate (see also Fig. 4). Identification of 3-EPB in both crystal forms prompted us to re-examine the published crystallographic data for *Sc*MqnA (12), solved prior to identification of the futalosine pathway. Unbiased difference electron density shows clearly the presence of 3-EPB in all four chains in the deposited data (Fig. S5). In all three crystal forms, 3-EPB is completely buried between the two lobes (see Movie S1), where it is held in place by hydrophobic contacts (to Ile13, Pro41, Val78, Val84, Cys87, Ile150, Phe186, Ala187) and multiple polar interactions to amino acids that are highly conserved in MqnA (Figs. 2, *B*, *C* and S6).

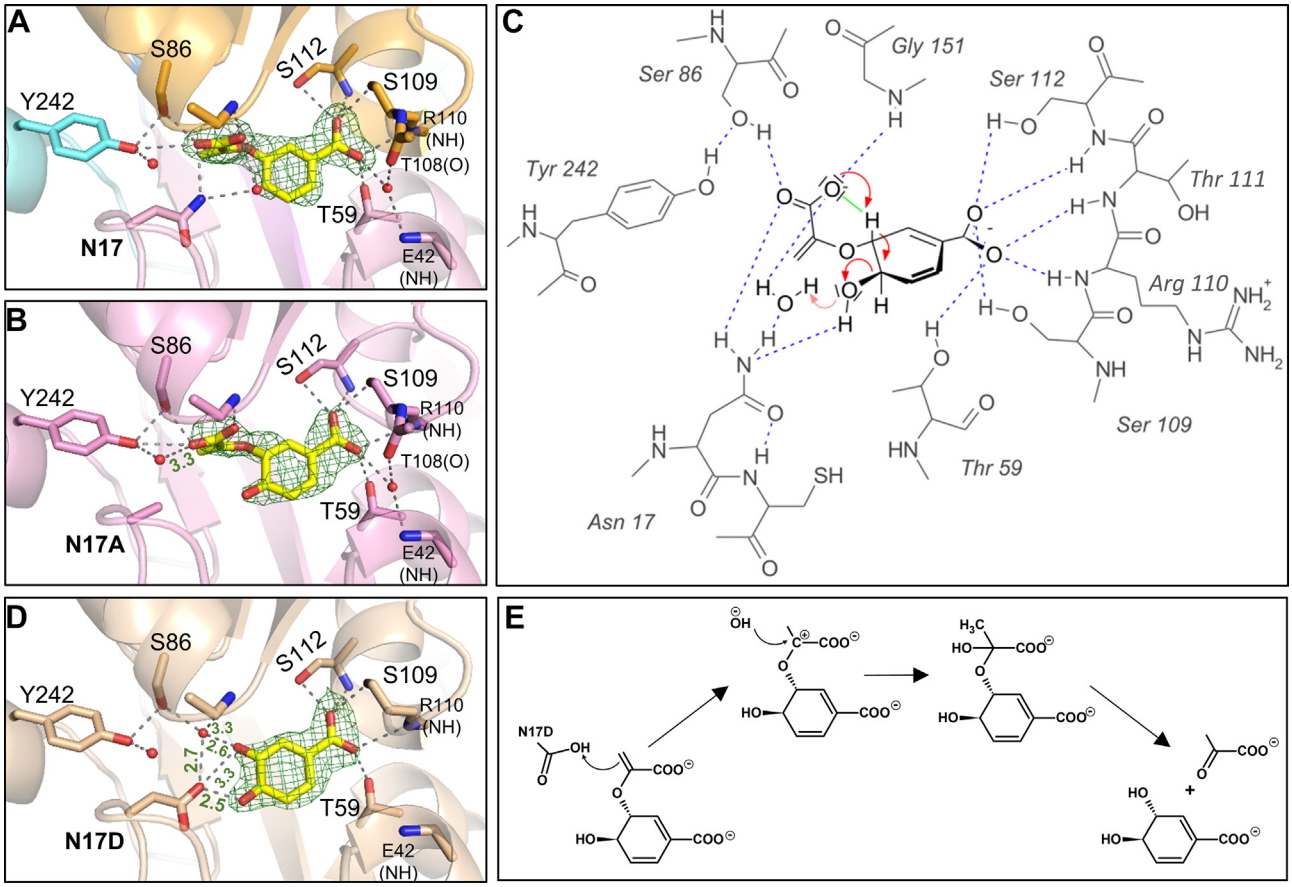

Figure 3. Active sites of *Sc*MqnA and its mutants with bound ligands reveal the mechanism of dehydration. The omit Fo-Fc electron density (contoured at 3σ) of the ligand is shown as *green mesh*, hydrogen bonds are represented as *black dashed lines*, and ordered solvent molecules near the active site ligands are shown as *red spheres*. Distances that differ with respect to wild type (see also Fig. 2*B*) are indicated (Å). *A*, wildtype *Sc*MqnA with co-purified 3-enolpyruvyl-benzoate (3-EPB); *B*, *Sc*MqnA mutant Asn17Ala with soaked chorismate; *C*, proposed mechanism of chorismate dehydration by MqnA *via* substrate-assisted catalysis. Departure of the hydroxy leaving group might be facilitated by deprotonation of a water molecule bound to Asn17 (displayed by *pink arrow*); *D*, *Sc*MqnA mutant Asn17Asp with omit Fo-Fc electron density interpreted as 3,4-dihydroxycyclohexa-1,5-dienoate (3,4-CHD); *E*, putative mechanism of chorismate hydrolysis by the *Sc*MqnA mutant Asn17Asp, analogous to that of the chorismate hydrolase (chorismatase) FkbO (21). *Sc*MqnA, MqnA from *Streptomyces coelicolor*.

No positively charged side chains contact either of the two 3-EPB carboxylate groups. Instead, both are positioned at the N termini of two α-helices (the benzoate carboxy group near α3 and α4, and the enol pyruvyl group near α1 and α6), allowing compensation of their negative charges by the positive poles of the α-helices. In comparison to the synthetic ligand 3-HBA(13), 3-EPB is positioned deeper in the active site (Fig. S7). Neither of the carboxy groups superimpose on that of the benzoate carboxy group of 3-HBA; instead, an acetate ion from the crystallization buffer for *Dr*MqnA occupies the position of the 3-EPB enol pyruvyl carboxylate, which is oriented by strong hydrogen bonds to the side chains of Asn17 and Ser86 (*Sc*MqnA numbering), both of which are absolutely conserved in MqnA (Fig. S7), and to the main chain amide of Gly151. Tyr242, located ∼3.5 Å from the carboxy group of the enol pyruvyl substituent, forms a hydrogen bond with the side chain of Ser86 and may therefore help to orient Ser86 for 3-EPB binding. In addition, the 3-EPB benzoate carboxy group makes hydrogen bonds to the side chains of Thr59 and Ser109 and to main chain atoms of Arg110, Thr111, and Ser112 of the mobile loop mentioned above. Significantly, the binding site is only partially occupied in the less ordered orthorhombic chain A (Fig. S4*C*), suggesting that 3-EPB binding draws residues of lobe 2 toward the active site. Finally, two ordered water molecules make hydrogen bonds to the carboxy groups of 3-EPB (Fig. 2*C*).

Identifying the catalytic base reveals substrate-assisted dehydration

Remarkably, there are no ionizable side chains in the proximity of the aromatic ring of 3-EPB that could act as catalytic base or acid during dehydration. The enol pyruvyl group of the product is however fixed by hydrogen bonds in an orientation that positions the carboxylate oxygen O13 in hydrogen bonding distance to C3 of 3-EPB (2.8–3.0 Å). Consequently, chorismate dehydration could proceed *via* substrate assisted elimination through deprotonation of C3 by the enol pyruvyl group. To test this hypothesis, we investigated the effect of mutating Asn17, Ser86, and Tyr242. Mutants Asn17Asp, Asn17Ser, and Ser86Ala showed low activity in an end-point assay run over 3 h and no detectable activity in a

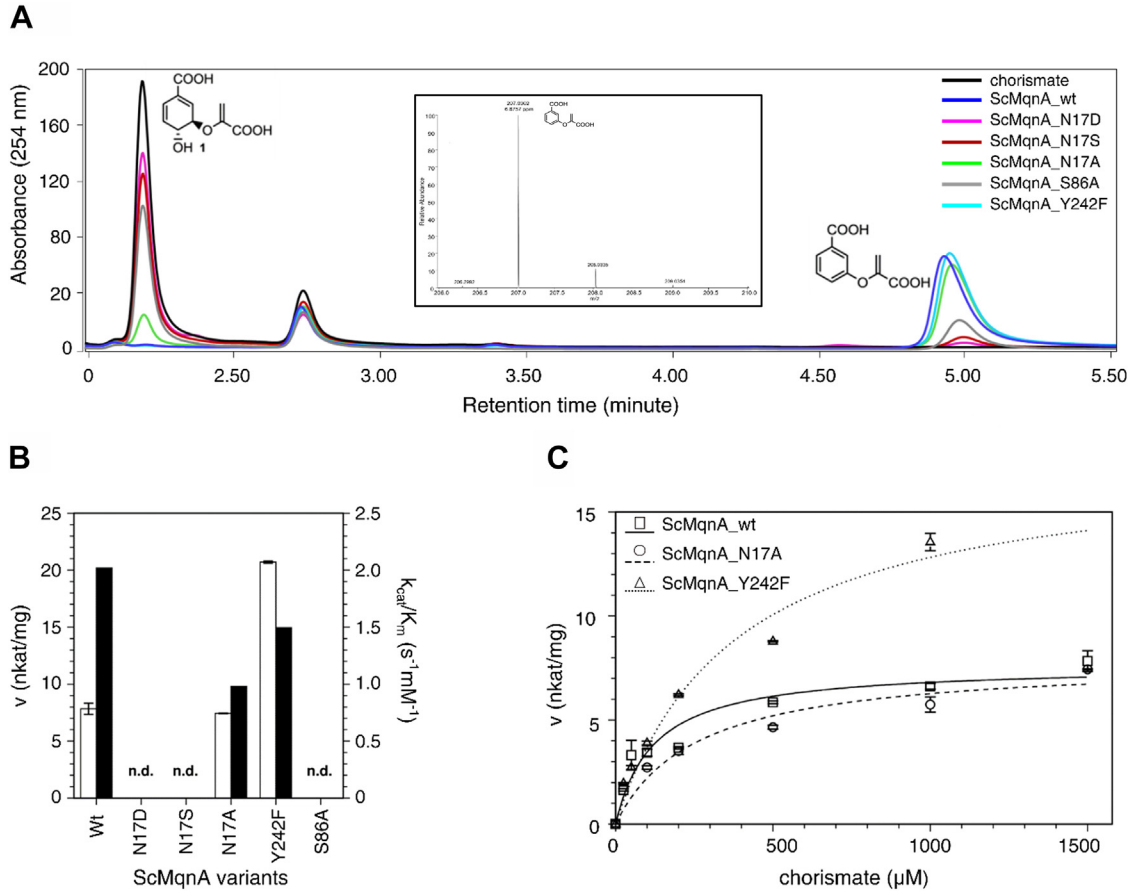

Figure 4. Enzymatic activity screening and kinetic study of ScMqnA and its mutants. *A*, HPLC chromatograms of initial screening of enzymatic activity. The chromatograms were recorded after 3 h of incubation of individual enzymes and chorismate. ScMqnA and the mutants are shown in different colors as indicated on the right top corner of the chromatogram. Inset: Mass spectrum identifying product as 3-EPB. *B*, comparison of the catalytic velocity (v, *white bars*) at 1500 μM chorismate concentration as well as the catalytic efficiency (k_{cat}/K_m, *black bars*) of ScMqnA and its mutants. *C*, substrate-velocity curves for ScMqnA and its mutants. Each data point was measured three times (n = 3). *Sc*MqnA, MqnA from *Streptomyces coelicolor*.

kinetic assay (Fig. 4 and Table 1). The Asn17Ala mutant showed no significant change in velocity but a 2-fold increase of the K_m value in the kinetic assay, whereas the Tyr242Phe mutant showed no reduction in activity in either assay.

Each of the mutants crystallized in the monoclinic space group, under slightly different conditions to those of wildtype *Sc*MqnA and with minor changes in the cell constants (Table S1). The overall structures of the mutants are almost identical to the wildtype and can be superimposed with r.m.sd values of ∼0.2 to 0.7 Å, with minor differences in the loops encompassing residues 107 to 110 and 133 to 136. Despite the lower activity of mutants Asn17Ala, Asn17Ser, and Ser86Ala, density for the product 3-EPB was clearly visible in each map (Fig. S8). Superposition of the Asn17Ala structure on that of the wildtype reveals an identical positioning of the product. In the Asn17Ser crystals, on the other hand, 3-EPB binds in two alternate conformations, one identical to that in WT *Sc*MqnA while the other exhibits a reorientated enol pyruvyl carboxy group that hydrogen bonds to the mutated Ser17 as well as to the side chain and main chain of Ser86. This conformation exhibits unfavorable distances and angles for proton transfer from C3 of the ring system, suggesting that the low activity of Asn17Ser is caused by improper positioning of the enol pyruvyl carboxy group. The 3-EPB aromatic ring system is tilted in the Ser86Ala mutant compared to the WT complex, with the enol pyruvyl carboxy group, which can no longer hydrogen bond to Ser86Ala due to the missing Ser86O$^{\gamma}$, shifted by ∼2 Å to hydrogen bond with Tyr242. Such a conformation would preclude substrate-assisted catalysis, explaining the observed low activity of the Ser86Ala mutant.

The *Sc*MqnA Asn17Ala crystals could be successfully soaked with chorismate using short incubation times of 2 to 3 min. Whereas the electron density of the enol pyruvyl group is not fully defined, probably due to the missing interaction with Asn17, the rest of the substrate clearly is (Fig. 3*B*). The enzyme-bound chorismate adopts a pseudodi*equatorial*

Table 1
Kinetic data for *Sc*MqnA and its mutants

Enzyme (mutant)	K_m (μM)	v_{max} (nkat/mg)	k_{cat} (s^{-1})
ScMqnA (wildtype)	121 ± 38	7.63 ± 0.65	0.24 ± 0.02
ScMqnA (Asn17Asp)	–	–	–
ScMqnA (Asn17Ser)	–	–	–
ScMqnA (Asn17Ala)	257 ± 87	7.88 ± 0.81	0.25 ± 0.02
ScMqnA (Ser86Ala)	–	–	–
ScMqnA (Tyr242Phe)	377 ± 106	17.65 ± 2.15	0.56 ± 0.06

Every datapoint was measured three times (n = 3), and standard errors were calculated by the fitting software. The kinetics of Asn17Asp, Asn17Ser, and Ser86Ala could not be determined due to their very weak activity in the assay.

conformation, the preferred conformation of chorismate in solution (18), in which the hydroxy-C4 bond and the enolpyruvyl-C3 bond are equatorial to the ring structure. This is in contrast to the otherwise so far universally observed pseudodi*axial* conformation adopted for catalysis in *e.g.*, chorismate mutase (19) or the isochorismate synthases MenF/EntC (20) (Fig. 5). Chorismate binds to *Sc*MqnA in a similar manner to 3-EPB, except for a slight shift of the enol pyruvyl group toward Phe242 caused by the puckering of the ring system. As observed for 3-EPB, the carboxylate oxygen O13 of chorismate is positioned in hydrogen bonding distance to chorismate C3 (on average 2.8 Å), which would allow it to act as a catalytic base accepting a proton from C3 (Fig. 3*C*). The complex structure is in agreement with the activity data that showed a velocity comparable to wild type MqnA and a reduced affinity that is likely to be caused by the missing hydrogen bond between substrate and Asn17.

Superposition of the Asn17Ala-chorismate structure onto that of wildtype *Sc*MqnA shows that no positively charged side chain is present near the leaving hydroxy group that could activate it by protonation. The Asn17 side chain nitrogen atom, however, would be in hydrogen bonding distance to the hydroxy group. Polarization of the C4-OH bond by the Asn17 side chain amide in combination with deprotonation of C3 by the enol pyruvyl carboxylate and the driving force of aromatization of the cyclohexadiene ring are probably sufficient to abstract the hydroxide, in agreement with the E1cb mechanism proposed by Mahanta *et al.* based on the observed MqnA activity at basic pH values (13). Additionally, a water molecule that is involved in a hydrogen bonding network *via* the enol pyruvyl group in wildtype *Sc*MqnA structures would form a hydrogen bond to the hydroxy group of chorismate and could thus further stabilize the evolving negative charge or even protonate the leaving hydroxy group.

Introduction of additional carboxylate results in alternative bound ligand

Surprisingly, positive difference electron density at the active site of mutant Asn17Asp corresponded to neither chorismate nor 3-EPB, neither of which were detected by LC-MS/MS analysis (Fig. S4). Instead, the ligand could be modeled as 3,4-CHD, a hydrolysis product of chorismate (21) together with an ordered solvent molecule (Fig. 3*D*). Compared to 3-EPB and chorismate, 3,4-CHD shows a small but significant shift toward the side chain of Asn17Asp, with the two hydroxyl groups within hydrogen bonding distance of Asn17Asp$O^{\delta 2}$ and a new water molecule bridging 3,4-CHD O11, Asn17Asp$O^{\delta 2}$, Ser86O^{γ}, and backbone amide Gly151NH. As with 3-EPB, 3,4-CHD has not been detected as an *E. coli* metabolite (17), so that we likewise suggest that the ligand has been generated during expression of the Asn17Asp *Sc*MqnA mutant, remaining bound to and co-purified with the enzyme. Introduction of the Asn17Asp carboxy group in the immediate vicinity of the enolpyruvyl group would be sufficient to change the mechanism from a substrate-assisted dehydration reaction to an enzyme-catalyzed (albeit slow) hydrolysis (Fig. 3*E*). This would be tantamount to converting the enzyme into a chorismate hydrolase or chorismatase, with a mechanism analogous to that proposed for FkbO (21), for which a pseudodiaxial chorismate conformation has also been postulated.

Substrate entry and product release require active site opening

All our *Sc*MqnA complex structures, as well as the previously solved *Sc*MqnA structure (12), exhibit a closed, solvent inaccessible active site, raising the question of how substrate and product can access and leave the active site and what conformation is adopted by ligand-free *Sc*MqnA. Although we

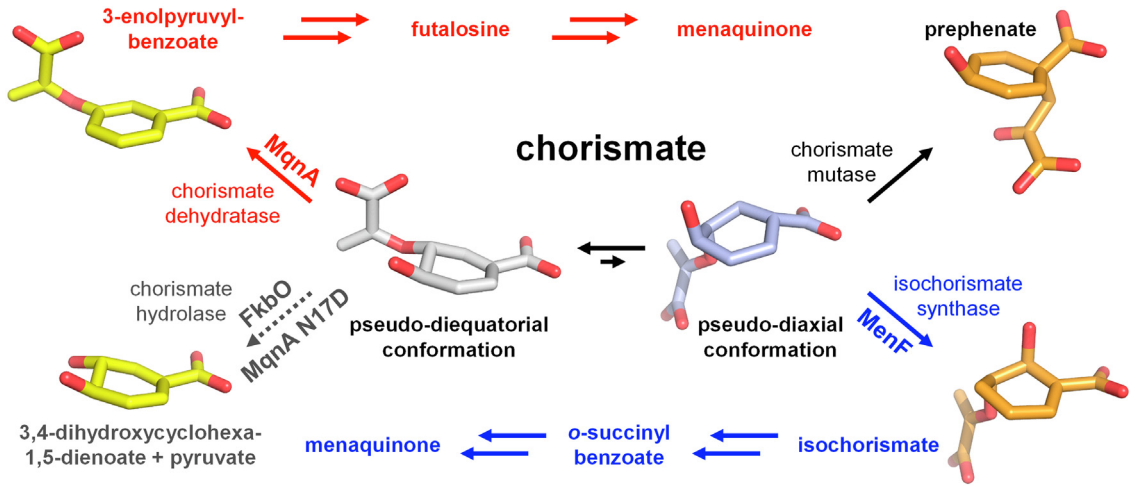

Figure 5. Conformations of chorismate found in the active sites of *Sc*MqnA (pseudo-diequatorial), chorismate mutase, and isochorismate synthase (both pseudo-diaxial) together with the corresponding products. The pseudo-diequatorial conformation of chorismate (the preferred conformation in solution (18)) found in MqnA fosters a compact form that is capable of intramolecular protonation and stabilization of the leaving hydroxy group by a water-mediated hydrogen bond to the enol pyruvyl group. In contrast, chorismate mutase binds chorismate in the pseudodiaxial conformation (19) (as do the isochorimate synthases MenF/EntC (20)), required for the Claisen rearrangement to take place *via* a chairlike transition resulting in conversion of chorismate to prephenate. *Sc*MqnA, MqnA from *Streptomyces coelicolor*.

were unable to obtain any ligand free crystals (in each case, a copurifying ligand was found in the active site), the active site of the orthorhombic A chain is only partially occupied by 3-EPB. This is accompanied by disorder of the region 109 to 112 and an upward movement of amino acids of lobe two including strand β7 and helix α5 (Fig. S3). Interestingly, a similar adjustment is observed comparing the two chains of the 3-HBA-*Dr*MqnA complex structure (13) (Fig. S9): Whereas the active site of chain A adopts a closed, solvent inaccessible conformation, that of chain B is open and solvent accessible, mainly due to a rearrangement of residues 107–111 (numbering according to *Sc*MqnA sequence), a small shift of helix α2 in lobe one and a slight outward rotation of the complete lobe 2.

A characteristic feature of VFT proteins is the ligand-mediated switching between an open ligand-free and a closed ligand-bound structure. This conversion is normally performed by a significant rigid body motion of one lobe relative to the other through changes in dihedral angles of amino acids in the hinge regions. Open and closed conformations of lysine/arginine/ornithine-binding protein and maltodextrin binding protein, for example, can be interconverted by a rotation of lobe two by 52° and 37°, respectively, without significant structural changes within the separate lobe domains (Fig. S10) (22–24). In contrast, the rotation angle between the two 3-HBA-*Dr*MqnA lobe domains (13) accounts only for 7°; in ligand-free *Dr*MqnA (pdb code 2i6e (12)), the eight independent chains exhibit states between these two conformations.

We postulate that an equilibrium exists between open and closed states of MqnA, with binding of the benzoate and enol pyruvate carboxy groups of the chorismate substrate/3-EPB product favoring the closed state. A comparable situation has been observed in the chorismate converting MST enzymes (25) (Fig. S1), in which a magnesium ion binds to the benzoate carboxy group of chorismate and thereby closes the active site pocket (20). Opening of the *Sc*MqnA active site can be seen as a combined result of local conformational changes—especially of the 109 to 112 region—and a slight rotation of the two lobes. Interestingly, other VFT enzymes, such as desulfinase DszB (26), thiaminase I, and thiamin pyrimidine synthase Thi5 (27, 28), also show local rearrangements of loops and α-helices at the opening of the active site, with negligible motion of the two lobes toward each other. Taken together, these observations suggest that enzymes exploit the ligand-binding properties of the VFT fold for specific substrate binding and catalysis but restrict conformational changes largely to the immediate proximity of the active site.

Ligand-mediated conformational switching is utilized by cognate ABC transporters to differentiate between loaded and unbound periplasmic binding proteins (29). In analogy, it is conceivable that the conformational rearrangements in MqnA, facilitating the complete burial of substrates and products with accompanying topological changes to the surface of the enzyme, could play a role in substrate/product channeling from and to other enzymes of the biosynthetic pathway.

Experimental procedures

Cloning, overexpression, and purification of recombinant ScMqnA

The *mqnA* gene from *S. coelicolor* (strain ATCC BAA-471/A3(2)/M145; UniProt Q9L0T8) was amplified by PCR using genomic DNA obtained from DSMZ Braunschweig as template and the forward and reverse primers (GGA ATT CCA TAT GGT GGA CAA TTC TCG CAC CCG G) and (CCG CTC GAG GGG CTT GAG CAG CTC GAC CT). The amplified DNA fragment was subcloned into NdeI/XhoI digested pET21a. After transformation of the plasmid into Rosetta (DE3) *E. coli*, the cells were grown to an A_{600} of 0.6 to 0.8 at 37 °C in Luria-Bertani medium, cooled to 20 °C, and supplemented with 0.3 mM isopropyl 1-thio-β-D-galactopyranoside for induction of protein expression. The cells were harvested after overnight expression by centrifugation, resuspended in lysis buffer [50 mM Tris/HCl pH 8.0, 300 mM NaCl, 5% Glycerol, supplemented with benzonase-nuclease (Sigma-Aldrich) and protease inhibitor cocktail (Roche)] and then lysed by constant pressure cell disruption (Constant Systems Ltd). After centrifugation of the cell lysate for 1 h at 21,100*g*, the supernatant was applied to a 5 ml His-Trap-HP column (GE Healthcare) that was washed using wash buffer (50 mM Tris/HCl pH 8.0, 300 mM NaCl, 5% glycerol, 50 mM imidazole) before elution of MqnA with elution buffer (50 mM Tris/HCl pH 8.0, 300 mM NaCl, 5% glycerol, 100 mM imidazole). Eluted protein was further purified by size-exclusion chromatography using a Superdex200 10/300 column (GE Healthcare) equilibrated in 10 mM Hepes pH 7.5, 150 mM NaCl, 10% glycerol, 5 mM DTT. Protein concentrations were determined using the UV absorbance at 280 nm and the appropriate calculated molar absorption coefficients.

*Sc*MqnA mutants were generated by PCR amplification of the pET21a_MqnA plasmid using the primers harboring one single mutation (N17D primer: CAC ATC CAG TTC CTG GAC TGC CTG CCC CTG, N17S primer: CAC ATC CAG TTC CTG AGC TGC CTG CCC CTG, N17 A primer: CAC ATC CAG TTC CTG GCC TGC CTG CCC CTG, S86 A primer: AC GGC CCC GTG ATG GCG TGC GTG ATC GTC and Y242 F primer: C ACC CTG GCG AAG TTC TTC ACC ACC CTC G) and subsequent DpnI-digestion of the methylated template plasmid. After transformation of the reaction mixture into XL1-blue competent cells, clones that contained the desired mutations were identified by sequencing. The *Sc*MqnA mutants were purified using the same protocol as for the wildtype.

Crystallization, data collection, and structure determination

Purified *Sc*MqnA and its mutants (10 mg/ml) were screened for crystallization conditions using sitting drop vapor diffusion with a crystallization robot (Cartesian) in 96-well plates (SWISSCI MRC Crystallization plates). Initially obtained small crystals were optimized by hanging drop vapor diffusion in 15 well plates (Qiagen). Crystals appeared overnight at 20 °C under a variety of conditions (Table S1) and grew for 1 to

2 days. For soaking experiments, crystals of ScMqnA mutants were soaked with 10 mM of chorismate in crystallization solution at 10 °C for less than 3 minutes, as crystals tended to dissolve after longer times.

Prior to data collection, crystals were flash frozen in liquid nitrogen, with some needing cryoprotection (20% (v/v) glycerol). Diffraction data were collected in-house at 100 K with Cu Kα radiation (λ = 1.5418 Å) using a CCD detector (Saturn 944+, Rigaku/MSC) mounted on a rotating anode generator (Micromax 007, Rigaku/MSC). All crystals diffracted in the range of 1.7 to 2.0 Å (Table S1). X-ray diffraction data were indexed and integrated using XDS (30) and the structures solved by the molecular replacement method using Phaser-MR (31). The previously published *Sc*MqnA structure (PDB entry: 2NXO) (12) was used as a search model to solve the orthorhombic ($P2_12_12_1$) wild type structure, and chain B of this used as search model for the monoclinic crystal forms. Structures were refined by iterative model building in Coot (32) and refinement using phenix_refine (33). All structure figures were generated using PyMOL (Schrödinger, LLC). Data collection and refinement statistics are listed in Table S1.

Identification of co-purified–bound ligands

Purified protein was concentrated to 30 to 50 mg/ml and mixed 1:1 with a 6M guanidine chloride solution to denature the protein. After centrifuging 100 µl of the mixture through a 1 ml Vivaspin column (10 kD cutoff), the flow through was diluted 10 times before being subjected to LC-MS/MS analysis using an Agilent 1290 LC system connected to an API 3200 triple quadrupole mass spectrometer equipped with a TurboIon ion source (AB Sciex). The analytes were separated on a Nucleoshell C18 column (2.6 µm, 50 × 3 mm; Macherey-Nagel) at 30 °C at a flow rate of 500 µl min^{-1} using 0.2% (v/v) acetic acid in water or acetonitrile as eluents A and B, respectively. The percentage of B was linearly increased from 0% to 25% over 4 min and thereafter to 98% B over 1 min. After 2 min at 98% B, the starting conditions were restored over 1 min, and the column was allowed to re-equilibrate for 1 min. The ion source was operated in the negative mode at a curtain gas pressure of 30 psi, an ion source voltage of -4500 V, a temperature of 450 °C, and sheath and de-solvation gas pressures of 50 psi, respectively. Data were acquired in the multiple reaction monitoring mode (Q1 and Q3 set at unit resolution) with a target scan time of 50 ms. N_2 was used as collision gas with a pressure of 5 psi. Multiple reaction monitoring transitions for each compound as well as compound specific instrument parameters are shown in Table S2. Collision-induced dissociation mass spectra were recorded at a collision potential of −20 V.

End-point activity screen for ScMqnA_wt and mutants

300 µM of ScMqnA and its mutants were incubated at room temperature for 3 h with 2 mM of chorismate (C1716; Sigma-Aldrich) in 100 mM Tris/HCl, pH 7.5. The enzyme was removed using Vivaspin 1 ml tubes (GE Healthcare) with a cutoff of 10 kDa. The product formed in all the reactions was purified by HPLC (UltiMate3000 Thermo Scientific) as described by Mahanta *et al.* (11). Product formation was monitored by following the increase in absorbance at 254 nm. The product peak was identified by LC-MS as described above.

MqnA kinetics assay using LC-MS/MS

All assays were conducted with substrate concentrations of 0 to 1500 µM and enzyme concentration of 0.05 µM in 50 µl of total reaction buffer (100 mM Tris/HCl, pH 7.5). The reaction mixture was incubated at room temperature (22 °C) for 5 min and quenched by addition of 50 µl of 6 M guanidium chloride. Nine hundred microliter of 100% methanol was added to the reaction mixture followed by centrifugation at 21,100*g* for 30 min to remove any precipitate. Ten microliter of the supernatant was taken for LC-MS. LC-MS/MS analysis was performed as described above. Peak areas were calculated using the IntelliQuant algorithm of the Analyst 1.6.2 software (AB Sciex) and manually adjusted if necessary. All subsequent calculations were performed with Excel (Microsoft Office Professional Plus 2010). Kinetic parameters were determined by fitting the data to the Michaelis-Menten equation using the nonlinear least-squares fitting program in FigP (Fig.P Software Incorporated).

Association state of ScMqnA analyzed by analytical ultracentrifugation

*Sc*MqnA at protein concentrations of 0.02 to 1 mg/ml in 10 mM Hepes, pH 7.5, 150 mM NaCl, 5 mM DTT, and 10% (v/v) glycerol was analyzed using a Beckman Optima XL-I centrifuge equipped with an An50Ti rotor and double sector cells. Sedimentation equilibrium measurements were carried out at 20 °C and 12,000 rpm, sedimentation velocity was monitored for 3 h at 40,000 rpm, 20 °C every 10 min. The data were recorded at a wavelength of 280 nm and analyzed using the software Sedfit (34). Buffer density was measured to 1.026 g/ml.

Sequence alignment and conservation analysis

Sequence alignment was performed using Clustal Omega tool (35) for multiple sequence alignment and EsPript 3.0 (36).

Data availability

The structures presented in this paper have all been deposited in the Protein Data Bank with the codes 7AHR, 7AN5, 7AN6, 7AN7, 7AN8, and 7YWC (Table S1). All remaining data are contained within the article.

Supporting information—This article contains supporting information.

Author contributions—A. P., C. B., and M. T. S. conceptualization; A. P., D.-A. N., H. L., and J. Z. investigation; A. P. methodology; A. P. data curation; A. P. writing-original draft; C. B. and M. T. S. writing-reviewing and editing; M. T. S. funding acquisition; M. T. S. supervision.

Funding and additional information—This work was supported by the Landesforschungsschwerpunkt Sachsen-Anhalt "Molekulare Biowissenschaften als Motor der Wissensbasierten Ökonomie" (Fkz. ZS/2016/06/79740) to M. T. S.

Conflicts of interest—The authors declare that they have no conflicts of interest with the contents of article.

Dedication—Dedicated to Professors Robert Huber and Wolfram Bode on the occasions of their 85th and 80th birthdays, respectively.

Abbreviations—The abbreviations used are: 3-EPB, 3-enolpyruvyl-benzoate; 3-HBA, 3-hydroxy-benzoate; 3,4-CHD, 3,4-dihydroxycyclohexa-1,5-dienoate; *Dr*MqnA, MqnA from *Deinococcus radiodurans*; *Sc*MqnA, MqnA from *Streptomyces coelicolor*; VFT fold, Venus flytrap fold.

References

1. Fujimoto, N., Kosaka, T., and Yam, M. (2012) Menaquinone as well as ubiquinone as a crucial component in the Escherichia coli respiratory chain. In *Chemical Biology*, InTech, London, UK: 187–208
2. Collins, M. D., and Jones, D. (1981) Distribution of isoprenoid quinone structural types in bacteria and their taxonomic implications. *Microbiol. Rev.* **45**, 316–354
3. Berkner, K. L. (2005) The vitamin K–dependent carboxylase. *Annu. Rev. Nutr.* **25**, 127–149
4. Dairi, T. (2012) Menaquinone biosyntheses in microorganisms. *Met. Enzymol.* **515**, 107–122
5. Bentley, R., and Meganathan, R. (1982) Biosynthesis of vitamin K (menaquinone) in bacteria. *Microbiol. Rev.* **46**, 241–280
6. Hiratsuka, T., Furihata, K., Ishikawa, J., Yamashita, H., Itoh, N., Seto, H., *et al.* (2008) An alternative menaquinone biosynthetic pathway operating in microorganisms. *Science* **321**, 1670–1673
7. Zhi, X.-Y., Yao, J.-C., Tang, S.-K., Huang, Y., Li, H.-W., and Li, W.-J. (2014) The futalosine pathway played an important role in menaquinone biosynthesis during early prokaryote evolution. *Genome Biol. Evol.* **6**, 149–160
8. Dairi, T. (2009) An alternative menaquinone biosynthetic pathway operating in microorganisms: an attractive target for drug discovery to pathogenic Helicobacter and Chlamydia strains. *J. Antibiot.* **62**, 347–352
9. Seto, H., Jinnai, Y., Hiratsuka, T., Fukawa, M., Furihata, K., Itoh, N., *et al.* (2008) Studies on a new biosynthetic pathway for menaquinone. *J. Am. Chem. Soc.* **130**, 5614–5615
10. Joshi, S., Fedoseyenko, D., Mahanta, N., Manion, H., Naseem, S., Dairi, T., *et al.* (2018) Novel enzymology in futalosine-dependent menaquinone biosynthesis. *Curr. Opin. Chem. Biol.* **47**, 134–141
11. Mahanta, N., Fedoseyenko, D., Dairi, T., and Begley, T. P. (2013) Menaquinone biosynthesis: formation of aminofutalosine requires a unique radical SAM enzyme. *J. Am. Chem. Soc.* **135**, 15318–15321
12. Tyagi, R., Burley, S. K., and Swaminathan, S. (2007) X-ray structures of two proteins belonging to Pfam DUF178 revealed unexpected structural similarity to the DUF191 Pfam family. *BMC Struct. Biol.* **7**, 62
13. Mahanta, N., Hicks, K. A., Naseem, S., Zhang, Y., Fedoseyenko, D., Ealick, S. E., *et al.* (2019) Menaquinone biosynthesis: biochemical and structural studies of chorismate dehydratase. *Biochemistry* **58**, 1837–1840
14. Janin, J., Bahadur, R. P., and Chakrabarti, P. (2008) Protein–protein interaction and quaternary structure. *Q. Rev. Biophys.* **41**, 133–180
15. Felder, C. B., Graul, R. C., Lee, A. Y., Merkle, H.-P., and Sadee, W. (1999) The venus flytrap of periplasmic binding proteins: an ancient protein module present in multiple drug receptors. *AAPS Pharm. Sci.* **1**, 7–26
16. Dupré, E., Herrou, J., Lensink, M. F., Wintjens, R., Vagin, A., Lebedev, A., *et al.* (2015) Virulence regulation with venus flytrap domains: structure and function of the periplasmic moiety of the sensor-kinase BvgS. *PLoS Pathog.* **11**, e1004700
17. Sajed, T., Marcu, A., Ramirez, M., Pon, A., Guo, A. C., Knox, C., *et al.* (2016) Ecmdb 2.0: a richer resource for understanding the biochemistry of *E. coli*. *Nucl. Acids Res.* **44**, D495–D501
18. Copley, S. D., and Knowles, J. R. (1987) The conformational equilibrium of chorismate in solution: implications for the mechanism of the non-enzymic and the enzyme-catalyzed rearrangement of chorismate to prephenate. *J. Am. Chem. Soc.* **109**, 5008–5013
19. Chook, Y. M., Gray, J. v, Ke, H., and Lipscomb, W. N. (1994) The monofunctional chorismate mutase from Bacillus subtilis. Structure determination of chorismate mutase and its complexes with a transition state analog and prephenate, and implications for the mechanism of the enzymatic reaction. *J. Mol. Biol.* **240**, 476–500
20. Meneely, K. M., Sundlov, J. A., Gulick, A. M., Moran, G. R., and Lamb, A. L. (2016) An open and shut case: the interaction of magnesium with MST enzymes. *J. Am. Chem. Soc.* **138**, 9277–9293
21. Hubrich, F., Juneja, P., Müller, M., Diederichs, K., Welte, W., and Andexer, J. N. (2015) Chorismatase mechanisms reveal fundamentally different types of reaction in a single conserved protein fold. *J. Am. Chem. Soc.* **137**, 11032–11037
22. Duan, X., and Quiocho, F. A. (2002) Structural evidence for a dominant role of nonpolar interactions in the binding of a transport/chemosensory receptor to its highly polar ligands. *Biochemistry* **41**, 706–712
23. Quiocho, F. A., Spurlino, J. C., and Rodseth, L. E. (1997) Extensive features of tight oligosaccharide binding revealed in high-resolution structures of the maltodextrin transport/chemosensory receptor. *Structure* **5**, 997–1015
24. Oh, B. H., Pandit, J., Kang, C. H., Nikaido, K., Gokcen, S., Ames, G. F., *et al.* (1993) Three-dimensional structures of the periplasmic lysine/arginine/ornithine-binding protein with and without a ligand. *J. Biol. Chem.* **268**, 11348–11355
25. Shelton, C. L., and Lamb, A. L. (2018) Unraveling the structure and mechanism of the MST(ery) enzymes. *Trends Biochem. Sci.* **43**, 342–357
26. Lee, W. C., Ohshiro, T., Matsubara, T., Izumi, Y., and Tanokura, M. (2006) Crystal structure and desulfurization mechanism of 2′-Hydroxybiphenyl-2-sulfinic acid desulfinase. *J. Biol. Chem.* **281**, 32534–32539
27. Coquille, S., Roux, C., Fitzpatrick, T. B., and Thore, S. (2012) The last piece in the vitamin B1 biosynthesis puzzle. *J. Biol. Chem.* **287**, 42333–42343
28. Sikowitz, M. D., Shome, B., Zhang, Y., Begley, T. P., and Ealick, S. E. (2013) Structure of a *Clostridium botulinum* C143S thiaminase I/thiamin complex reveals active site architecture. *Biochemistry* **52**, 7830–7839
29. Dwyer, M. A., and Hellinga, H. W. (2004) Periplasmic binding proteins: a versatile superfamily for protein engineering. *Curr. Opin. Struct. Biol.* **14**, 495–504
30. Kabsch, W. (2010) Xds. *Acta Crystallogr. D Biol. Crystallogr.* **66**, 125–132
31. Adams, P. D., Afonine, P. V., Bunkóczi, G., Chen, V. B., Davis, I. W., Echols, N., *et al.* (2010) Phenix: a comprehensive python-based system for macromolecular structure solution. *Acta Crystallogr. Sect. D: Biol. Crystallogr.* **66**, 213–221
32. Emsley, P., and Cowtan, K. (2004) Coot: model-building tools for molecular graphics. *Acta Cryst.* **60**, 2126–2132
33. Terwilliger, T. C., Grosse-Kunstleve, R. W., Afonine, P. V., Moriarty, N. W., Zwart, P. H., Hung, L. W., *et al.* (2008) Iterative model building, structure refinement and density modification with the PHENIX AutoBuild wizard. *Acta Crystallogr. D Biol. Crystallogr.* **64**, 61–69
34. Schuck, P. (2000) Size-distribution analysis of macromolecules by sedimentation velocity ultracentrifugation and lamm equation modeling. *Biophysi. J.* **78**, 1606–1619
35. Madeira, F., Park, Y. M., Lee, J., Buso, N., Gur, T., Madhusoodanan, N., *et al.* (2019) The EMBL-EBI search and sequence analysis tools APIs in 2019. *Nucl. Acids Res.* **47**, W636–W641
36. Robert, X., and Gouet, P. (2014) Deciphering key features in protein structures with the new ENDscript server. *Nucl. Acids Res.* **42**, W320–W324